PHYSICAL REVIEW B **72**, 165415 (2005)

Mechanisms of decomposition of metal during femtosecond laser ablation

Changrui Cheng and Xianfan Xu*
School of Mechanical Engineering, Purdue University, West Lafayette, Indiana 47907, USA

(Received 2 July 2004; revised manuscript received 14 June 2005; published 17 October 2005)

The mechanisms of decomposition of a metal (nickel) during femtosecond laser ablation are studied using molecular dynamics simulations. It is found that phase explosion is responsible for gas bubble generation and the subsequent material removal at lower laser fluences. The phase explosion process occurs as combined results of heating, thermal expansion, and the propagation of tensile stress wave induced by the laser pulse. When the laser fluence is higher, it is revealed that critical point phase separation plays an important role in material removal.

DOI: 10.1103/PhysRevB.72.165415 PACS number(s): 61.80.Az, 02.70.Ns, 79.20.Ds

I. INTRODUCTION

Pulsed laser ablation is the process of material removal after the target is irradiated by intensive laser pulses. It is now acknowledged that pulses with very short durations, such as picosecond or femtosecond, are advantageous in many applications.[1] The short pulse duration confines heat diffusion, which leads to high-quality machining. Sharp-edged, clean and highly reproducible machining results have been obtained using a femtosecond laser.[2]

Femtosecond laser ablation has become one of the most intensively investigated topics in the research of laser-material interaction. However, the basic mechanisms leading to ablation are still not conclusive. Femtosecond laser ablation occurs at very short temporal and spatial scales, involving complicated optical, thermodynamic, energy transfer, and mechanical processes which are closely coupled. At the same time, the target could be heated to extremely high temperature and pressure, where thermal and mechanical properties of the material are generally unknown.

Different mechanisms, such as phase explosion,[3–8] critical point phase separation,[9] spallation,[6] and fragmentation[7,8,10] have been proposed to explain the laser ablation process. Phase explosion is homogeneous bubble nucleation close to the spinodal temperature (slightly below the critical temperature), during which gas bubble nucleation occurs simultaneously in a super-heated, metastable liquid. The temperature-density (T-ρ) and pressure-temperature (p-T) diagrams of the phase explosion process are illustrated in Fig. 1.[3] During rapid laser heating, the liquid can be raised to a temperature above the normal boiling temperature (point A), which is in a state of superheating in the region between the binodal line and the spinode line on the phase diagram, the metastable zone. When the material approaches the spinode (point B), intense fluctuation could overcome the activation barrier for the vapor embryos to grow into nuclei. This activation barrier decreases as the material gets closer to the spinode, causing a drastic increase of the nucleation rate which turns the material into a mixture of vapor and liquid droplets. Therefore, spinode line is the limit of superheating in the metastable liquid, and no homogeneous structure will exist beyond it when the liquid is heated. Experimental work has shown that phase explosion occurred during nanosecond laser ablation of a metal.[4,11]

During femtosecond laser ablation, an important factor that needs to be considered is the extraordinary heating rate. Heating above the critical temperature directly from the solid phase becomes possible (point A in Fig. 2), followed by expansion leading to the thermodynamically unstable region (B), causing material decomposition.[12] This material decomposition process, from solid to supercritical fluid to the unstable region is termed critical point phase separation. Critical point phase separation induced by laser heating was studied using a one-dimensional Lagrangian hydrodynamic code.[9] It was found that the peak temperature of the liquid material exceeds the critical temperature during the initial heating period, then decreases to below the critical temperature while the material keeps its homogeneity and crosses the

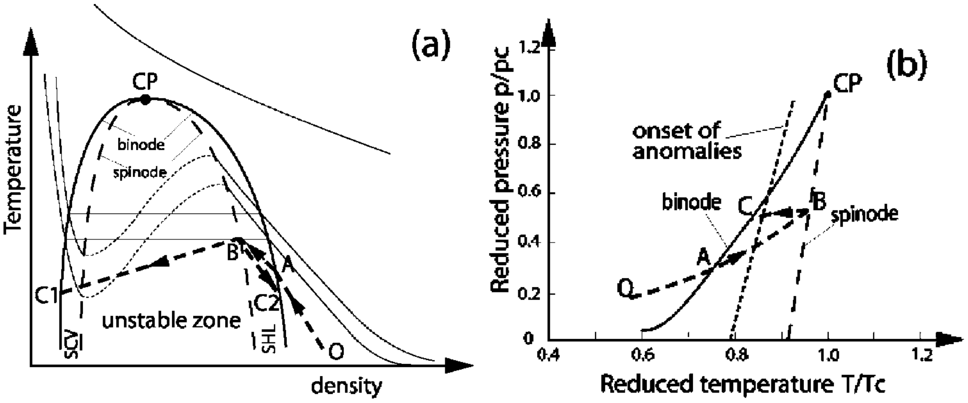

FIG. 1. (a) T-ρ and (b) p-T diagrams of phase explosion. Dome in solid line is the binode. Dome in dashed line is spinode. SHL, super-heated liquid. SCV, super-cooled vapor. CP, critical point.

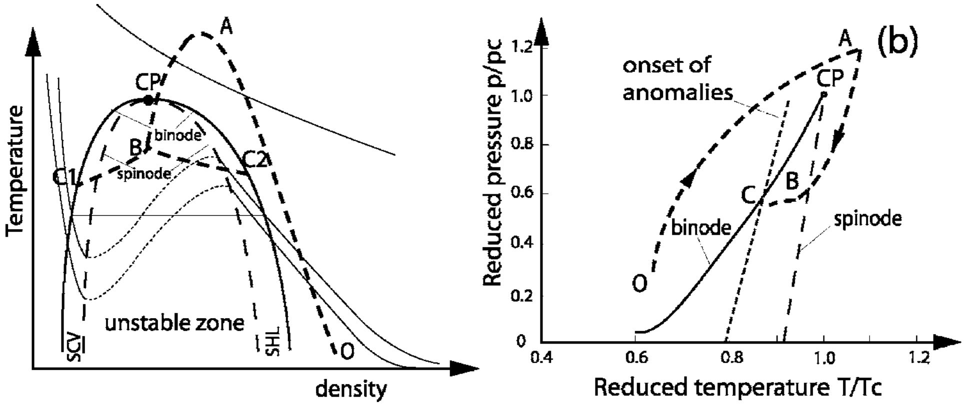

FIG. 2. (a) T-ρ and (b) p-T diagrams of critical point phase separation.

spinode line into the unstable zone, causing phase separation. Laser ablation of silicon was studied using a scheme combining Monte Carlo and molecular dynamics,[8] which showed phase explosion occurs in femtosecond laser ablation (500 fs). The same study showed for a 50 ps pulse, laser ablation is due to fragmentation caused by highly nonuniform strain rates or the instability in low-density liquids. However, different trends were observed in another molecular dynamics (MD) study.[6] A longer laser pulse (150 ps) leads to phase explosion, while using a shorter laser pulse (15 ps), the laser induced tensile stress has a strong effect on ablation. The inconsistency among the results in the literature could be due to the different fluence range, pulse width, materials studied, and the computational methods used.

Experimental measurements of transient parameters during femtosecond laser ablation such as temperature and pressure are highly challenging. In this work, we focus on molecular dynamic simulation of femtosecond laser ablation of nickel, and investigate possible ablation mechanisms at different laser fluences. Nickel is modeled as a system of atoms interacting via Morse potential, and molecular dynamics simulations are performed on this model system. The laser pulse width is fixed at 100 fs, the pulse width of the commonly used Ti:sapphire femtosecond laser. The detailed laser ablation process will be illustrated, and the ablation phenomena together with the thermodynamic paths of materials at different locations during ablation will be analyzed to identify the ablation mechanisms. To locate the thermodynamic paths, calculations of the critical point and binode line are conducted. As will be seen, we show that at lower laser fluences, phase explosion can be the dominant mechanism for femtosecond laser ablation, and critical point phase separation occurs at higher laser fluences.

II. SIMULATION METHODS

A. Molecular dynamics modeling

The problem studied in this work is femtosecond laser ablation of nickel in vacuum. The target has a thickness (in the x direction) of 187 nm, and a lateral dimension of 10.6 nm × 10.6 nm. Note that the length of the material will increase when it is heated, as will be seen in Sec. III. On the other hand, the MD simulation is capable of tracking motions of atoms due to thermal expansion and ablation. The laser pulse is incident along the x direction onto the target. It has a uniform spatial distribution and a temporal Gaussian distribution of 100 femtoseconds full width at half-maximum (FWHM) centered at $t=1$ picosecond. The wavelength of the laser is 800 nm.

In our MD model, the Morse potential[13] is used to simulate the interactions among atoms in nickel,

$$\Phi(r_{ij}) = D[e^{-2b(r_{ij}-r_{\varepsilon})} - 2e^{-b(r_{ij}-r_{\varepsilon})}], \tag{1}$$

where D is the total dissociation energy, r_{ε} is the equilibrium distance, and b is a constant, with values of 0.4205 eV, 0.278 nm, and 14.199 nm^{-1}, respectively.[13] Although there are other potentials suitable for metals, such as the embedded-atom method (EAM),[14] the Morse potential is chosen in this work because it has been proven to be a good approximation to the interactions between atoms in fcc metals such as nickel, and is capable of predicting many material properties. It has been widely used to study the laser-metal interaction in different laser applications.[15–18] Its simple form allows us to compute a relative large number of atoms, which is essential for revealing the details of the laser ablation process.

The procedure of the MD calculation is described as follows. At each time step, the total force, velocity, and position of all the atoms are calculated. The force vector acted on atom i from atom j is

$$\vec{F}_{ji} = F(r_{ji})\vec{r}^{\,o}_{ji} = -\frac{\partial\Phi(r_{ji})}{\partial r}\vec{r}^{\,o}_{ji} = 2Db(e^{-2b(r_{ji}-r_{\varepsilon})} - e^{-b(r_{ji}-r_{\varepsilon})})\vec{r}^{\,o}_{ji}, \tag{2}$$

where $\vec{r}^{\,o}_{ji}$ is the unit vector of $\vec{r}_{ji}$, the position vector from j to i. The total force on atom i is the summation of the force vectors from all neighboring atoms. After the total force for each atom is obtained, the velocity and position at the new time step are calculated from the modified Verlet algorithm.[19,20]

From Eq. (2), it is seen that the force between two atoms becomes negligible when they are very far away from each other. A cutoff distance, r_c (taken as 2.46 r_{ε} in this work), is therefore selected and the force between two atoms is evaluated only when their distance is less than r_c. The distances between atoms and r_c are compared using the cell structure and linked list method.[19,20] To avoid the time consuming evaluation of the forces using Eq. (2), a force table is precalculated, and the force between two atoms is obtained from this table according to their distance. The simulation speed is significantly increased by using these methods.

In this work, all the parameters are nondimensionalized to minimize the truncation errors. The total number of atoms is about 1 900 000 and a parallel processing technique is applied to accelerate the computation. A computer cluster composed of eight 2.0 GHz PCs is used. MPICH, a potable implementation of message passing interface, the standard for message-passing libraries, is applied for the parallel MD calculation. More details of the numerical approach are available elsewhere.[21]

B. Evaluation of thermodynamic parameters

In this work, precise evaluation of the thermodynamic parameters of material is crucial to the investigation of ablation mechanisms. The methods to calculate the temperature, pressure, and density are explained in this section.

The macroscopic parameters can be evaluated after the force-velocity-position of all atoms are obtained. To evaluate these parameters, the calculation domain is divided into layers perpendicular to the x direction. In this work, the thickness of the layers is the cutoff distance r_c. This means that temperature, pressure, density, etc., of the material are averaged in y-z cross sectional areas, and are functions of the x coordinate at each time step.

As will be shown in Sec. II C, the two-temperature model is applied, and the lattice and electrons of metals are considered as two systems having their own temperatures. The lattice temperature T_l is calculated by summing the kinetic energy, with the bulk velocity of the material excluded,

$$T_l = \frac{1}{3Nk_B} m \sum_{i=1}^{N} \left(\sum_{j=1}^{3} (v_{i,j} - \overline{v_j})^2 \right), \tag{3}$$

where N is the total number of atoms in a volume where the temperature is evaluated (about 10 000), k_B is the Boltzmann constant, and m is the mass of the atom. j represents the spatial coordinates (x, y, and z when $j=1$, 2 and 3, respectively), $v_{i,j}$ is the velocity of atom i at the jth coordinate, and $\overline{v_j}$ is the average velocity of the N atoms at the jth coordinate.

Pressure is another important quantity for the investigation of the thermodynamic processes during laser ablation. It is calculated using the expression[22]

$$p = \rho k_B T_l + \frac{1}{6V} \left\langle \sum_{i=1}^{N} \sum_{j \neq i} \vec{F_{ij}} \cdot \vec{r_{ij}} \right\rangle. \tag{4}$$

Equation (4) is derived from the virial theory, which considers the interaction of molecules in the matter to derive the equation of state. The first part ($\rho k_B T$) is from the momentum transport related to the random motion of the atoms, and is similar to the pressure in ideal gases where the forces between molecules and/or atoms are neglected. The second part $[(1/6V)\langle \sum_{i=1}^{N} \sum_{j\neq i} \vec{F_{ij}} \cdot \vec{r_{ij}} \rangle]$ considers the pressure from the interacting forces among atoms.

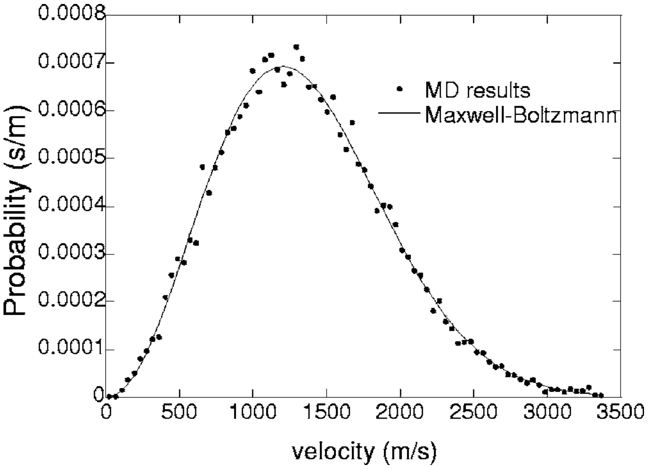

FIG. 3. The velocity distribution of the atoms at location $x=184.5$ nm and $t=120$ ps. Laser fluence is 0.3 J/cm^2.

In Eqs. (3) and (4), the volume with the lateral size of the material (10.6×10.6 nm) and the thickness of the cutoff distance is chosen to evaluate the temperatures and pressures. The number of atoms in such a volume ($\sim$10 000) is large enough to represent a Maxwell-Boltzmann velocity distribution [Eq. (5)], the theoretical equilibrium velocity distribution,

$$P(v) = 4\pi v^2 \left(\frac{m}{2\pi k_B T} \right)^{3/2} e^{-mv^2/2k_B T}. \tag{5}$$

An example is given in Fig. 3. The Maxwell-Boltzmann velocity distribution of the atoms indicates that the local equilibrium is established so that a temperature can be defined. Similar calculations under other times and laser fluences show that the local equilibrium is also achieved as shown later in Figs. 15 and 20. This is consistent with other work where a local equilibrium was found in ultrafast laser heating.[23]

Proper boundary conditions are important to the simulation. On the top surface which is irradiated by the laser pulse, the free boundary condition is applied. Periodical boundary conditions are applied in the lateral directions (y and z). To prevent the reflection of pressure wave, the bottom boundary is subject to the so-called "nonreflecting boundary condition."[24] For this boundary condition, the force calculation of atoms near the boundary is specially treated so that their behavior is similar to those inside the material and the incoming pressure wave will pass through the boundary. This ensures that the ablation process will not be interfered with by the reflected pressure wave.

C. Two temperature model for laser heating

In general, three energy transfer stages during femtosecond laser irradiation of metals have been identified.[25] Initially, the free electrons absorb the energy from the laser. This stage is characterized by a lack of thermal equilibrium among the electrons. In the second stage, the electrons reach thermal equilibrium and the density of states can now be represented by the Fermi distribution. However electrons and the lattice are still at two different temperatures. In the final stage, electrons and the lattice reach thermal equilibrium and thermal diffusion carries the energy into the bulk. A two-temperature model to predict the nonequilibrium temperature distribution between electrons and the lattice during femtosecond laser irradiation of metals was first described by Anisimov *et al.*[26] Qiu and Tien[27] derived the two-temperature model from the Boltzmann transport equation. The two-temperature model looks at the heating mechanism as consisting of the absorption of laser energy by the electrons and heating of the lattice by electron-lattice interaction. It treats electrons and the lattice as two separate subsystems with different temperatures governed by respective equations. It has been concluded that if the laser pulse duration is much longer than the electron relaxation time which is of the order of 1 fs, the first stage of electron nonequilibrium can be ignored.[28] As such, the existence of nonequilibrium between the electrons and the lattice is more important for the study of femtosecond laser (typically ~100 fs) metal interaction, resulting in wide applications of the two-temperature model (e.g., Ref. [29]).

In the two-temperature model, the electron temperature T_e, and the lattice temperature T_l are subject to two coupled one-dimensional (1D) governing equations,

$$C_e \frac{\partial T_e}{\partial t} = \frac{\partial}{\partial x}\left(k_e \frac{\partial T_e}{\partial x}\right) - G(T_e - T_l) + S, \tag{6}$$

$$C_l \frac{\partial T_l}{\partial t} = G(T_e - T_l), \tag{7}$$

where C_e and k_e are volumetric specific heat and thermal conductivity of electrons, respectively. Their temperature dependencies are approximated as $C_e = \gamma T_e$, $\kappa_e = \kappa_{e,0} T_e / T_l$. $G(T_e - T_l)$ is the electron-lattice coupling term, which shows that the energy transfer from electrons to the lattice is proportional to their temperature difference. The values of $\kappa_{e,0}$, γ, and G are taken as 91 W/m K, 1.065×10^3 J/m^3 K^2, and 3.6×10^{17} W/m^3 K, respectively.[29,30] S is the laser heating source term expressed as

$$S = \frac{I_0}{t_p \sqrt{\pi}} \frac{1}{d} e^{-[(t - t_0)/t_p]^2} e^{-x/d}, \tag{8}$$

where t_p is the time constant determining the pulse duration, and t_0 is the time of the pulse center. To achieve a 100 fs FWHM pulse centered at 1 ps, the values of t_p and t_0 are 0.06 ps and 1 ps, respectively. d is the absorption depth with a value of 14 nm,[31] and I_0 is the absorbed laser fluence.

Equation (6) is solved using the TDMA (Tri-Diagonal Matrix Algorithm) method with the adiabatic boundary condition applied on both boundaries. The value of temperatures of electrons and the lattice in the coupling term, $G(T_e - T_l)$, is taken as those in the previous time step.

The lattice temperature is updated by scaling the velocities of all atoms (with bulk velocity excluded) by a factor $\sqrt{1 + G(T_e - T_l)\delta t / E_{k,t}}$ at each time step, where $E_{k,t}$ is the kinetic energy at the time t, and δt is the time step. This is equivalent to solving Eq. (7), the governing equation of the lattice equation in the two-temperature model. Lattice conduction is always considered in the MD simulation, although it is small compared with the electron conduction in a metal. Another method has been used in literatures to consider the electron-lattice coupling during laser heating,[32,33] where the energy coupling between the electrons and the lattice is considered as an additional term in the total force of each atom. However, it can be shown that these two methods are identical.

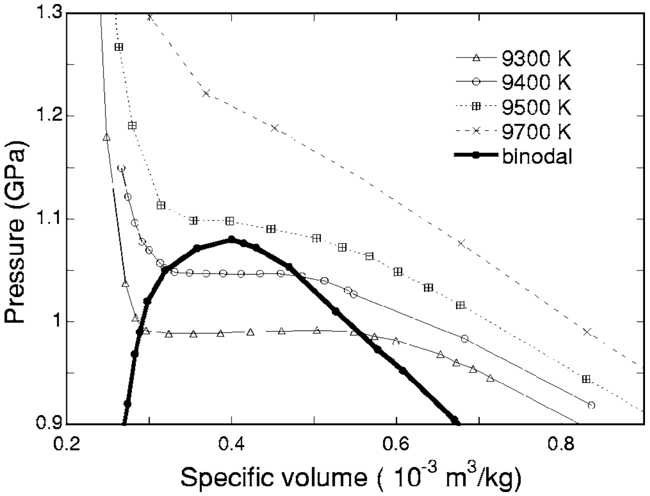

FIG. 4. Calculated *p-v* diagram near the critical point. Solid bold line is the binode.

To consider the effect of density variation from material expansion and phase change, thermal conductivity and specific heat of electrons are scaled by the ratio of the local density to the original density. Therefore, when density decreases, so do the effective thermal conductivity and specific heat. This is consistent with the electron properties of metals.[34] Before the heating calculation is started, the material is equilibrated at 300 K for about 300 ps to ensure it is under the expected initial equilibrium condition.

III. RESULTS

A. Evaluation of the critical point

Since we are interested in ablation around the critical point, we first evaluate the phase diagram, including the critical point and the binode line of our model system near the critical point. As will been seen, the phase diagram is crucial for analyzing the phase change mechanisms in laser ablation. The phase diagram is obtained by computing an equilibrium heating problem with periodical boundary conditions on all boundaries. At a fixed temperature, the pressure of the system as a function of specific volume is computed, that is, a *p-v* curve is obtained at each temperature. The system is equilibrated for a long time (200–300 ps) at each *p-v-T* value to ensure that the point on the phase diagram is at an equilibrium state. This is repeated at different temperatures, so *p-v* curves at different temperatures are obtained.

Figure 4 shows the results of the phase diagram and critical point calculation. It is seen that at 9700 K, the pressure decreases continuously with the increase of specific volume, indicating this temperature is above the critical temperature.

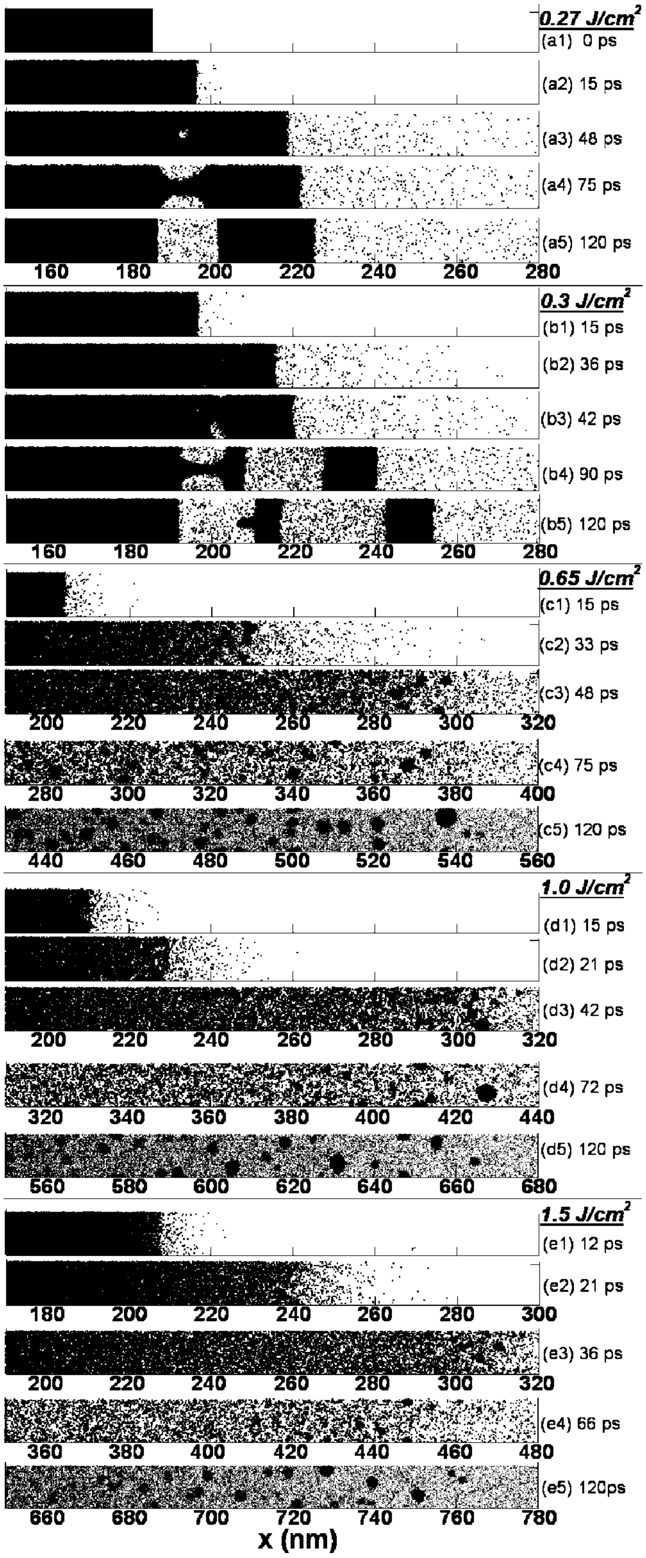

FIG. 5. Snapshots of the ablated area at different laser fluences and times.

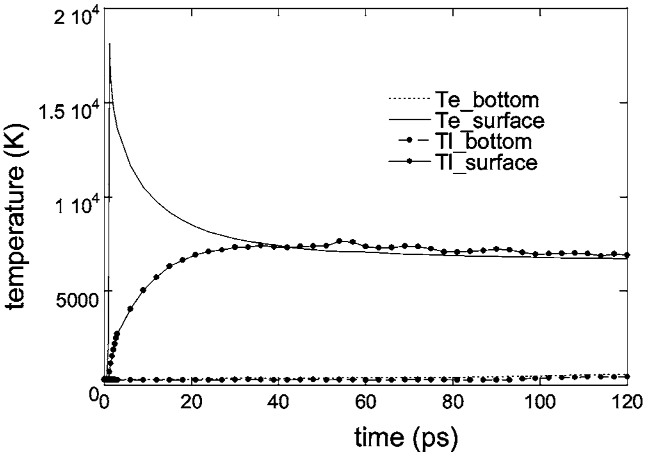

FIG. 6. Electron and lattice temperatures at the surface and the bottom of the target.

At 9300 K, the pressure does not decrease monotonously with the increase of specific volume; the flat plateau indicates the region where the liquid and vapor phases coexist which is confirmed by the observation of the two-phase structure. Therefore, the critical temperature is between 9700 K and 9300 K. More calculations at intermediate temperatures indicate that the parameters of the critical point are $T_c = 9470 \pm 40$ K, $\rho_c = 2500 \pm 200$ kg/m^3, and $p_c = 1.08 \pm 0.02$ GPa. The critical point of nickel found from literature is 9576 K/2293 kg/m^3/1.12 GPa,[35] 7810 K/2210 kg/m^3/0.49 GPa,[36] and 9284 K.[37] These values are extrapolated from low temperature data using semiempirical equations of state.

The binodal lines are obtained by connecting the points where the vapor phase starts to appear and where the liquid phase is turned into vapor completely. Between the binoldal lines, the pressure is a constant at a constant temperature, and liquid and vapor coexist as shown in Fig. 4.

In the following sections, the phase diagram obtained from the above calculation will be used to reveal the thermodynamic paths of the phase change processes during laser ablation.

B. Laser ablation

The process of laser ablation is first analyzed from the atomic distributions. Figure 5 shows snapshots of atomic distributions at laser fluences of 0.27, 0.3, 0.65, 1.0, and 1.5 J/cm^2. Here, only the near surface region where the laser energy is absorbed and laser ablation occurs is shown. In the figure, each atom is represented by a black dot. Laser is irradiated perpendicularly onto the right surface, while the bottom of the target is always located at $x = 0$ nm (not shown in the figure). To observe the interior of the target, the whole domain is sliced into 10 layers with equal thicknesses in the y direction, and the fifth layer is shown in these figures except Figs. 5(c5), (d5), and (e5), where the whole thickness is displayed. Note 0.27 J/cm^2 is the lowest laser fluence to cause volumetric phase change.

It is seen from these figures that the ablation phenomena are different at low and high fluences. At 0.27 J/cm^2 and 0.30 J/cm^2 [Figs. 5(a) and 5(b)], gas bubbles first appear inside the material, and grow larger at later time steps. After the size of bubbles is large enough, the material is separated into pieces. On the other hand, at higher laser fluences, the initial homogeneous phase turns into mixture of liquid drop-

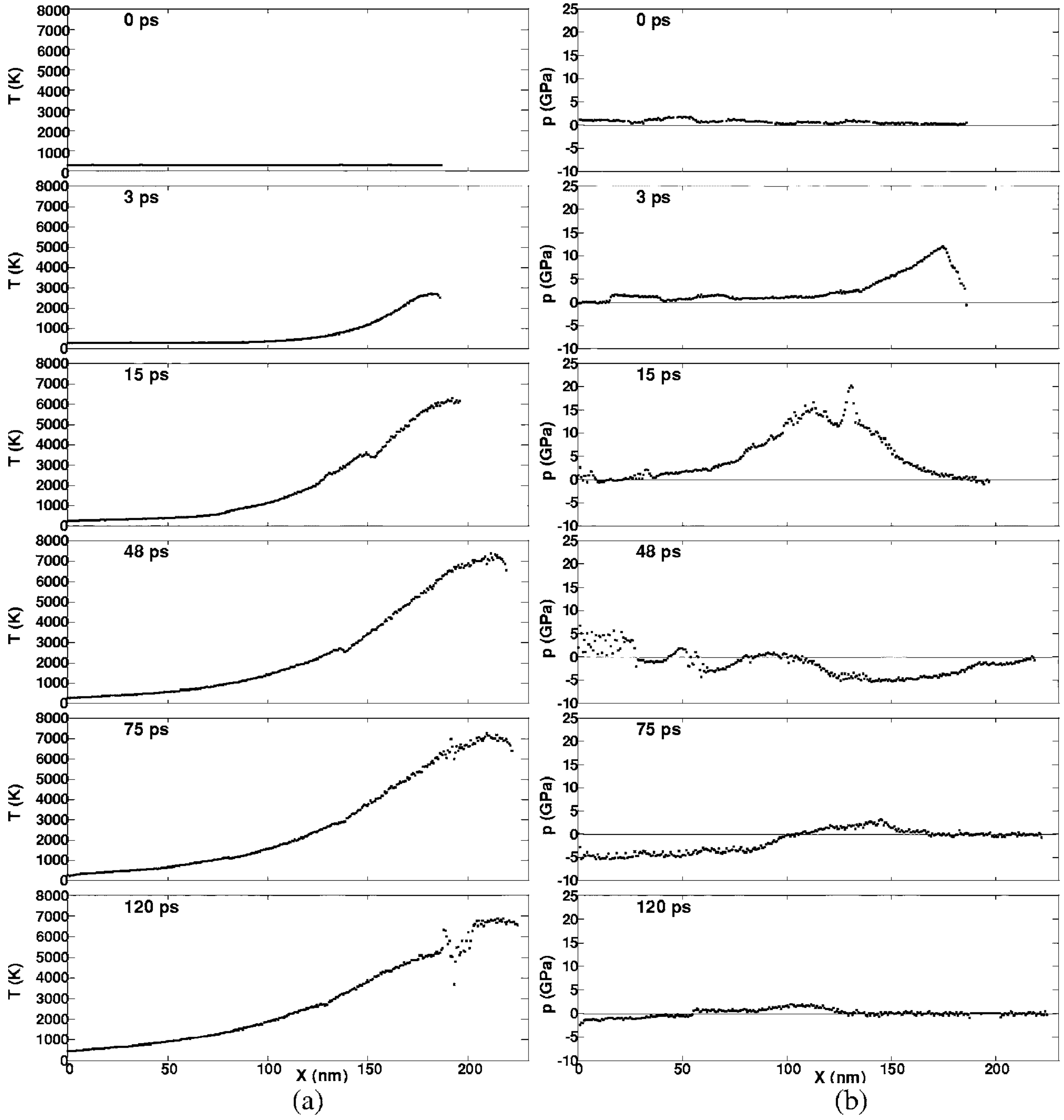

FIG. 7. (a) Temperature and (b) pressure distributions at different time steps at laser fluence of 0.27 $\mathrm{J/cm^2}$.

lets and gas phase over a long length, completely different from the low-fluence ablation where gas bubbles can be easily identified. The liquid droplets are then coalesced into bigger liquid clusters, while a certain number of atoms remain as the gas phase, forming a ″background″ vapor phase. We will point out in Sec. IV that different ablation patterns indicate different ablation mechanisms for low and high laser fluences.

Another phenomenon seen in Fig. 5 is that at the two lower laser fluences (0.27 $\mathrm{J/cm^2}$ and 0.30 $\mathrm{J/cm^2}$) the gas bubbles are generated inside the material, rather than on or near the surface. The distances from the surface to the origin of gas bubbles at laser fluences 0.27 and 0.3 $\mathrm{J/cm^2}$ are 25 and 18 nm, respectively. The reason why gas bubbles are generated inside the material will be discussed later in Sec. IV.

C. Time evolution of temperature, pressure, and density

The detailed ablation process is analyzed in this section by studying the time evolution of temperature, pressure, and density in the target material. The electron and the lattice temperature on the surface and the bottom of the material at the laser fluence of 0.27 $\mathrm{J/cm^2}$ are shown in Fig. 6. It is seen that the electron temperature on the surface is increased quickly to the peak value of 18 000 K, while the lattice temperature does not increase as fast. Due to the electron-lattice coupling, the electron temperature starts to decrease and the lattice temperature increases, until they reach approximately the same value after tens of picoseconds. The electron and lattice temperatures at the bottom stay constant at 300 K within 100 ps after the laser pulse.

The lattice temperature and pressure wave for the laser fluence of $0.27\ \mathrm{J/cm^2}$ at different time steps during the ablation process are shown in Fig. 7. Note that the laser pulse is centered at 1 ps with duration of 0.1 ps. At time 0, the target is at an equilibrium state of 300 K, and the pressure is almost zero. After the laser pulse is incident on the target, the surface temperature increases dramatically, and a strong compressive (positive) pressure is generated and propagates into the target. This compressive pressure is due to the thermal expansion in the near surface region. A negative pressure which represents a tensile stress follows the compressive wave, but its magnitude is much smaller. As will be shown later, this tensile stress has a significant effect on the material separation process. Melting occurs at the surface at about 6 ps. It is also noticed that the lattice temperature of the solid-liquid interface is about 3800 K, much higher than the calculated melting temperature of nickel (2500 K), indicating the existence of strong overheating. The interfacial temperature decreases at later time steps and reaches about 2750 K at 90 ps when the melting process slows down but does not stop. A lattice temperature disorder appears after 6 ps (for example, at about 150 nm at $t=15$ ps). Compared to the atomic distribution, it is found that this disorder always occurs at the liquid-solid interface; therefore, this temperature disorder is due to the energy transfer associated with solid-liquid phase change. The peak temperature reaches the highest value of 7700 K at 54 ps, lower than the critical temperature 9470 K calculated in Sec. III A.

The different phases of the material can also be revealed by the atomic number density distribution shown in Fig. 8, which is evaluated from dividing the number of atoms in a slice of material perpendicular to the depth direction x by the volume of this slot. For solid, the atomic density fluctuates from nearly zero to a high value along the x direction (see Fig. 8, 0 ps), since the density is high around the lattice layer but low in between the two lattice layers. Note that the thickness of the slice is much smaller than the lattice constant. For liquid, the atomic number density is almost uniform since there is no lattice structure (e.g., Fig. 8, 15 ps, 155–195 nm). For the gas state, since its density is much lower than that of the liquid, the number density would be small comparing with that of the liquid.

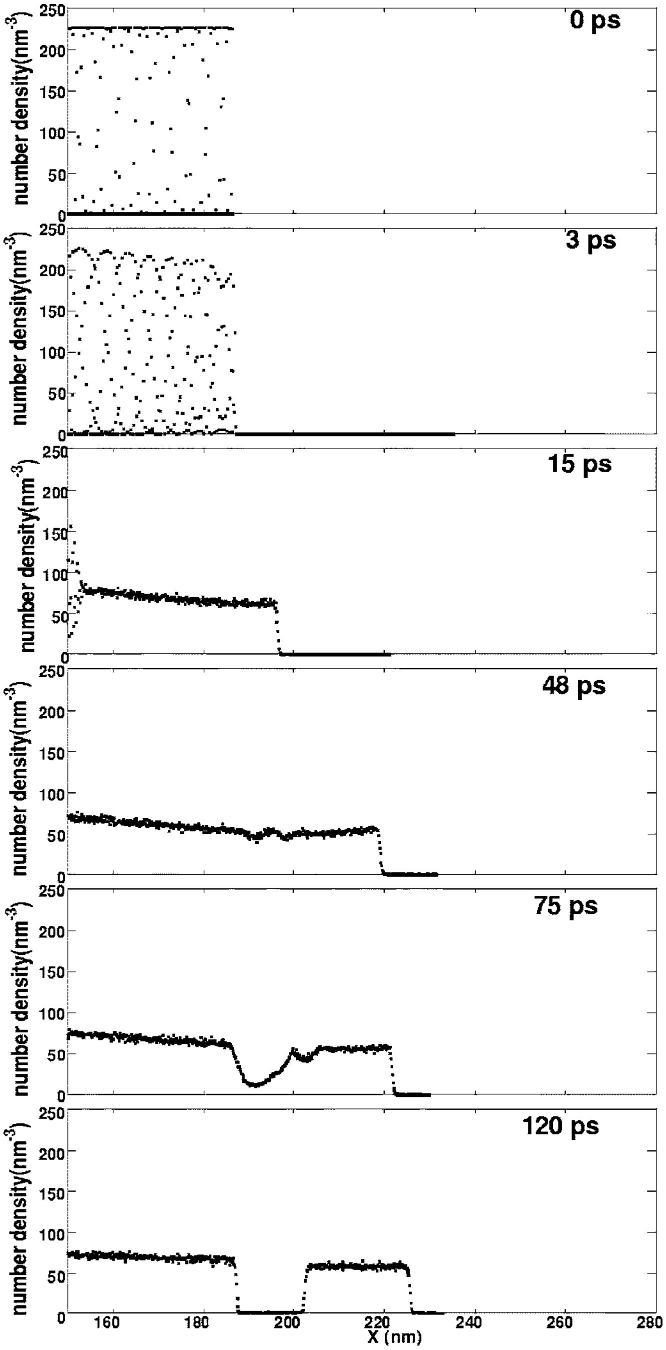

FIG. 8. Atomic number density at different time steps at laser fluence of $0.27\ \mathrm{J/cm^2}$.

The temperature and pressure distributions for other fluences of 0.30, 0.65, 1.0, and $1.5\ \mathrm{J/cm^2}$ are shown in Figs. 9, 10, 11, and 12, respectively. It is seen from these figures that the peak surface temperature increases significantly with the laser fluence, and even exceeds the critical temperature at three higher laser fluences (see Figs. 10–12). Also noted is that at these three laser fluences, the surface temperature is slightly lower than the interior temperature. As indicated in Fig. 5, expansion is very strong near the ablation front. Figures 7 and 9 show that the total thickness of the target increases 31 nm and 36 nm for $0.27\ \mathrm{J/cm^2}$ and $0.3\ \mathrm{J/cm^2}$, respectively, in about 45 ps after the laser pulse, while it increases 94 nm, 132 nm, and 152 nm for the three higher laser fluences. The stronger material expansion causes temperature decrease around the surface at higher laser fluences. As will be shown in Sec. IV, this cooling eventually leads to phase separation at these higher laser fluences, as compared to what happened at lower laser fluences when the phase change happens before significant cooling can take place.

Figures 9–12 reveal another important difference between

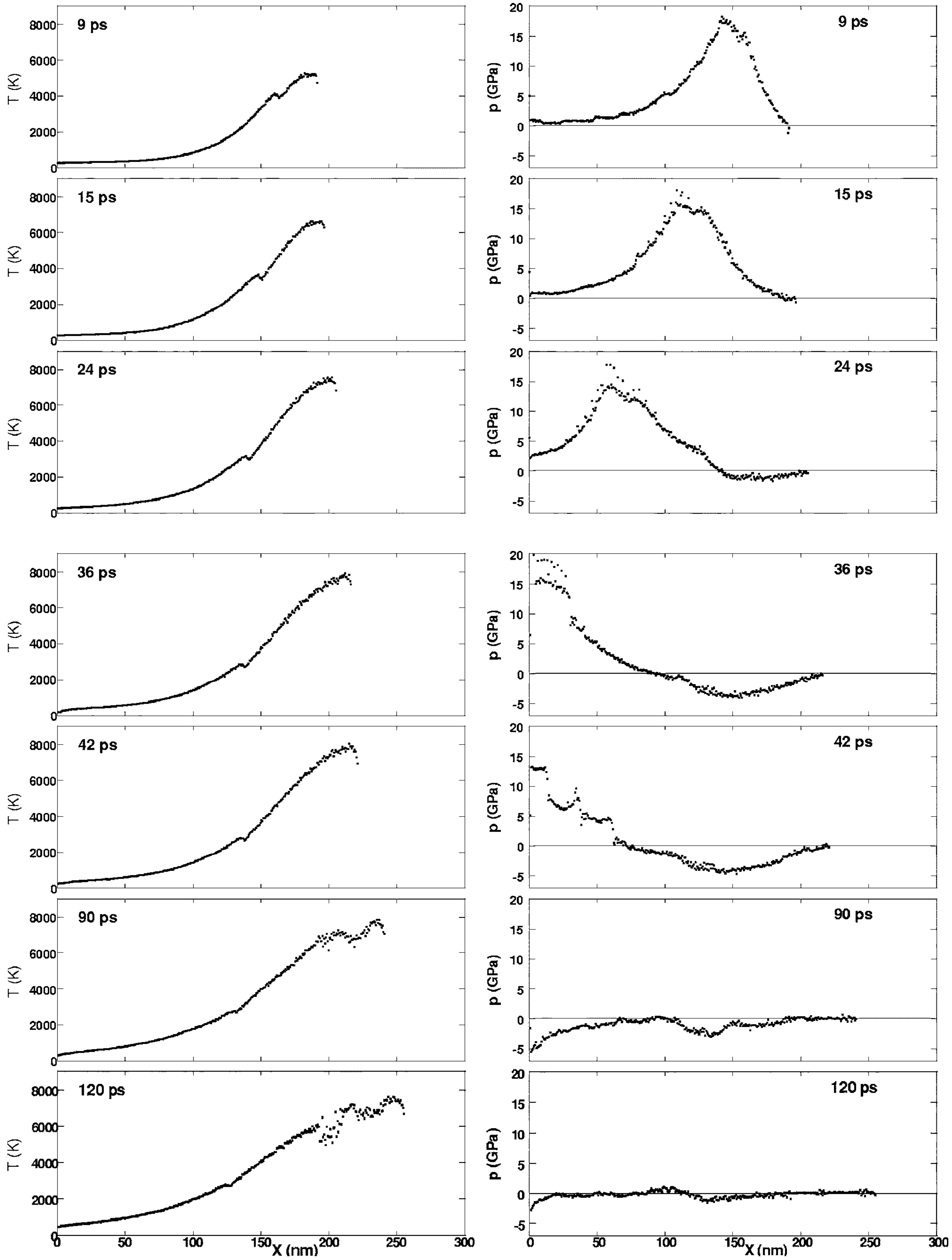

(a) (b)

FIG. 9. (a) Temperature and (b) pressure distributions at different time steps at laser fluence of 0.3 J/cm^2.

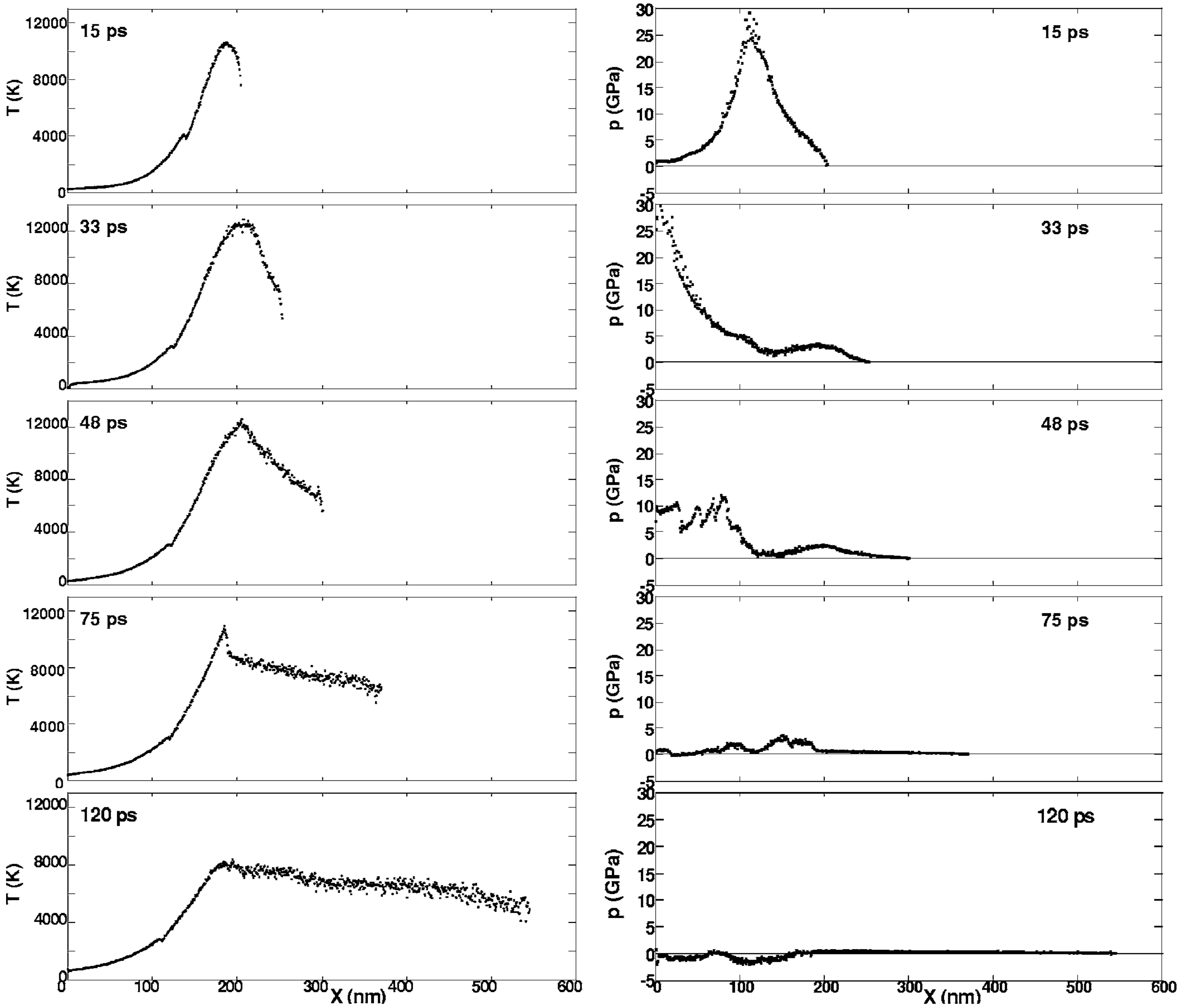

(a) (b)

FIG. 10. (a) Temperature and (b) pressure distributions at different time steps for fluence 0.65 J/cm^2.

the laser-material interactions at low and high laser fluences. As shown in Fig. 7(b), a tensile stress follows the compressive wave induced by laser heating at 0.27 J/cm^2. This tensile stress can also be observed for the fluence of 0.3 J/cm^2 in Fig. 9(b). However, for the three higher fluences of 0.65, 1.0, and 1.5 J/cm^2 shown in Figs. 10(b)–12(b), there is no such tensile stress following the compressive stress. The possible reason is that at these higher laser fluences, since the temperature near the surface is higher than the critical point, the material is a super-critical fluid with a low density. This low density super-critical fluid cannot withstand much tensile stress. It will be shown later in Sec. IV that the tensile stress assists the phase change process at lower laser fluences, while at higher laser fluences, phase separation occurs when the super-critical fluids enter the thermodynamic unstable zone as a result of expansion.

IV. DISCUSSIONS

A. Ablation at low laser fluences

The mechanisms leading to ablation is studied by analyzing the thermodynamic trajectories of groups of atoms that undergo phase separation. The thermodynamic trajectory represents the time evolution of the material under investigation in thermodynamic space. Specifically, the evolutions of groups of atoms in T-ρ diagrams are plotted and analyzed in details. There is no preference in choosing the groups of atoms. Atoms in one group are in close proximity to each other, and follow the bulk motion of the material. Atoms are allowed to enter or leave the group.

Figure 13 shows the groups of atoms analyzed for the laser fluence of 0.3 J/cm^2 at 120 ps [the same figure as Fig. 5(b5)]. According to Fig. 13, groups 2 and 4 have turned into

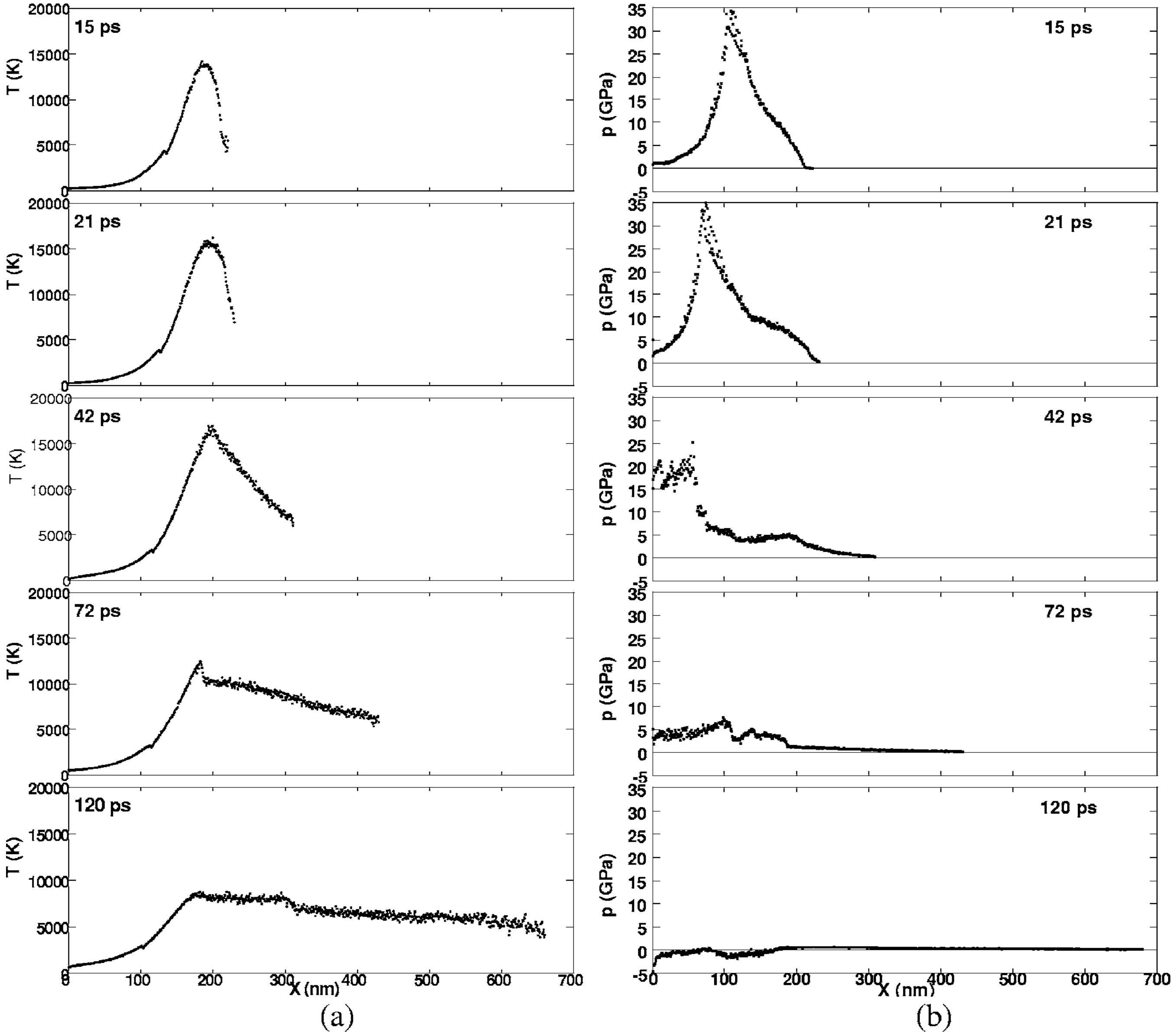

FIG. 11. (a) Temperature and (b) pressure distributions at different time steps at laser fluence of 1.0 J/cm^2.

gas at 120 ps, while groups 1, 3, and 5 are in the liquid phase (and will remain as liquid). Their thermodynamic trajectories of densities and temperatures during the ablation process are shown in Fig. 14. The arrows indicate the progress of time, while the numbers along the trajectories mark the time in ps. The binode and spinode lines are taken from the calculation results in Sec. III A. From Fig. 14, it is seen that groups 2, 3, and 4, which experience material separation, cross both the binode line and the spinode line. These three groups undergo a phase separation process, with groups 2 and 4 turning into vapor. On the other hand, groups 1 and 5, which do not touch the spinode, do not undergo phase change. This indicates that the phase change of the material is directly related to whether it reaches the spinode line or not. Recall what was described in Sec. I for phase explosion, when liquid enters the metastable region and approaches the spinode, it will undergo the phase explosion process and turn into a mixture of liquid and vapor. Therefore, the thermodynamic trajectories of the groups suggest that phase explosion occurs at this laser fluence.

In the above discussion, it is important that local thermal equilibrium is achieved so that a temperature can be defined. This can be verified by plotting out the velocity distribution at the locations of interest and comparing it with the equilibrium Maxwell-Boltzmann distribution expression, Eq. (5). In Fig. 15, the velocity distributions of atom groups 2 and 3 in Figs. 13 and 14 at a number of time steps leading to ablation are shown. The Maxwell-Boltzmann distributions that can best represent these velocity distributions are also shown. From Fig. 15, it is seen that velocities of atoms indeed follow the equilibrium Maxwell-Boltzmann distribution.

Analyzing the ablation process at a lower fluence of 0.27 J/cm^2 reaches the same conclusion, groups of atoms that are not able to reach the spinode line do not experience phase separation, while those crossing the spinodal line undergo phase separation.

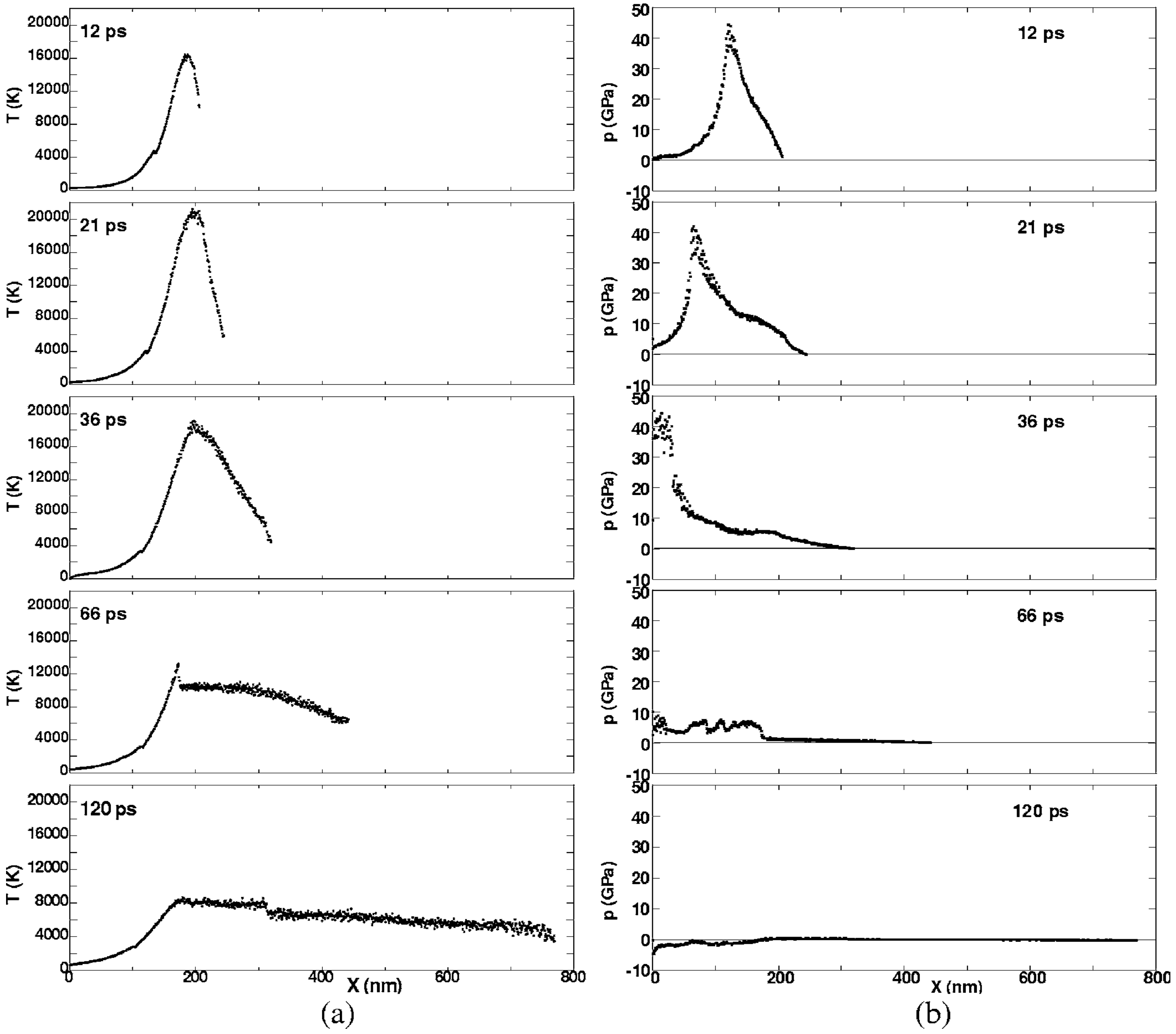

FIG. 12. (a) Temperature and (b) pressure distributions at different time steps at laser fluence of 1.5 J/cm^2.

At a lower laser fluence of 0.25 J/cm^2, no gas bubbles are generated. A number of groups of atoms are marked in the T-ρ diagram in Fig. 16 at the time steps when they are closest to the spinode line. Although the temperature of liquid is between 5500 K and 6900 K, much higher than the equilibrium boiling temperature (3186 K), none of these groups reach the spinode line and turn into vapor. Therefore, liquid vapor phase change does not occur at this laser fluence. This confirms again that crossing the spinode line is necessary for the material to turn into gas and experience decomposition.

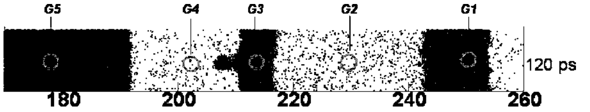

FIG. 13. Positions of groups of atoms at laser fluence of 0.3 J/cm^2.

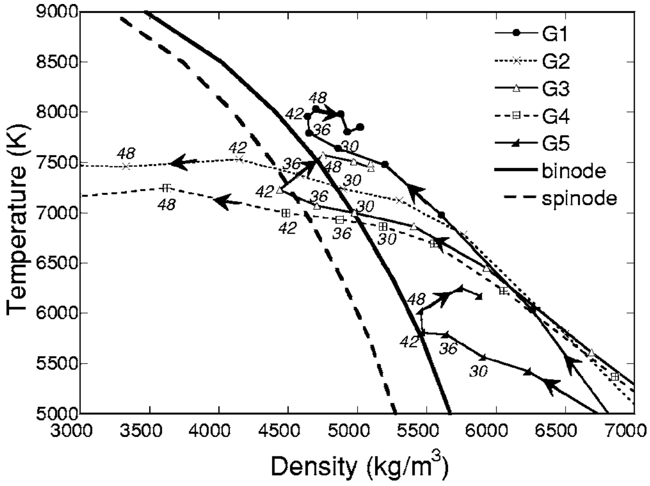

FIG. 14. Thermodynamic trajectories of groups of atoms at laser fluence of 0.3 J/cm^2.

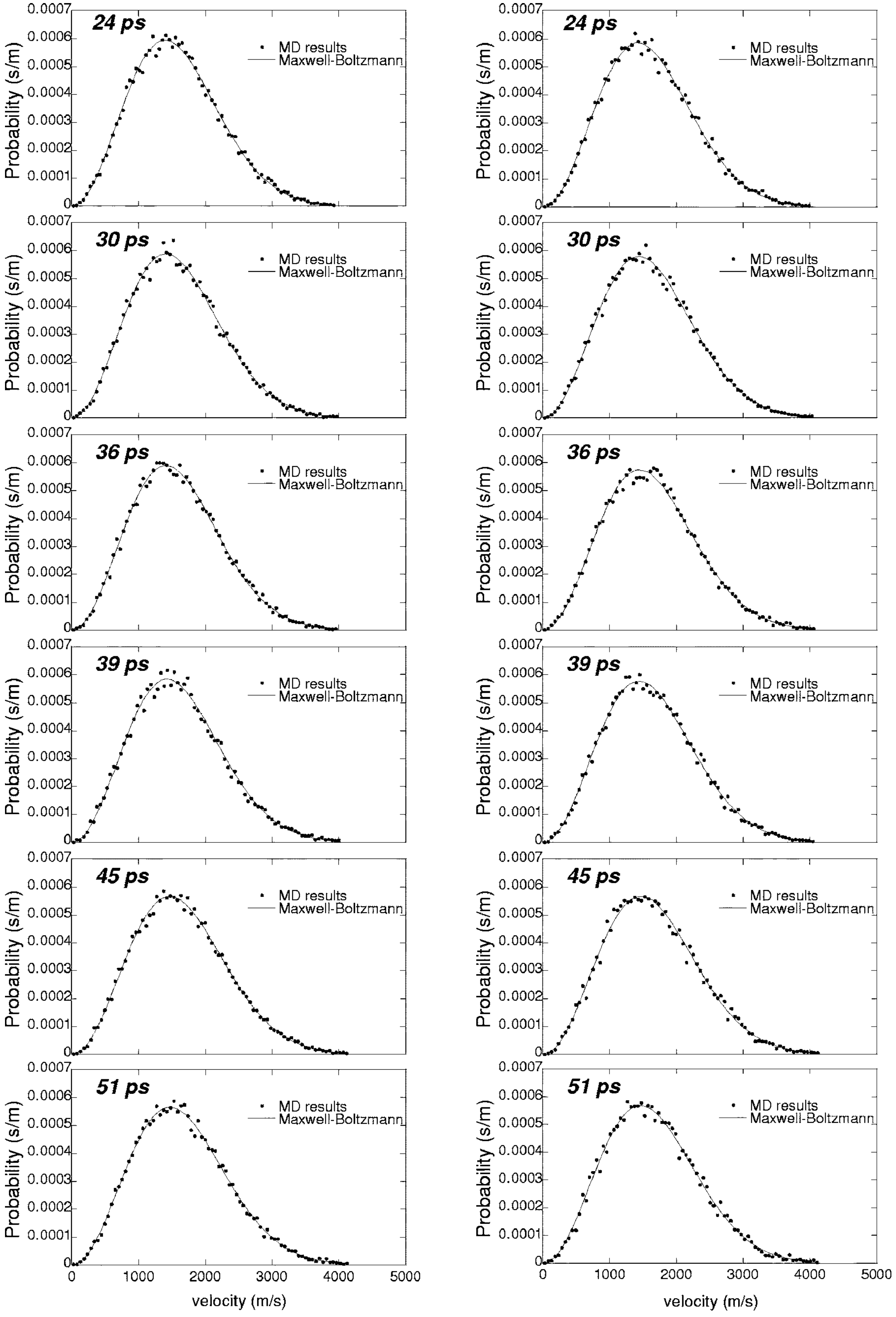

(a) (b)

FIG. 15. Velocity distributions for (a) group 3 and (b) group 2 in Figs. 13 and 14.

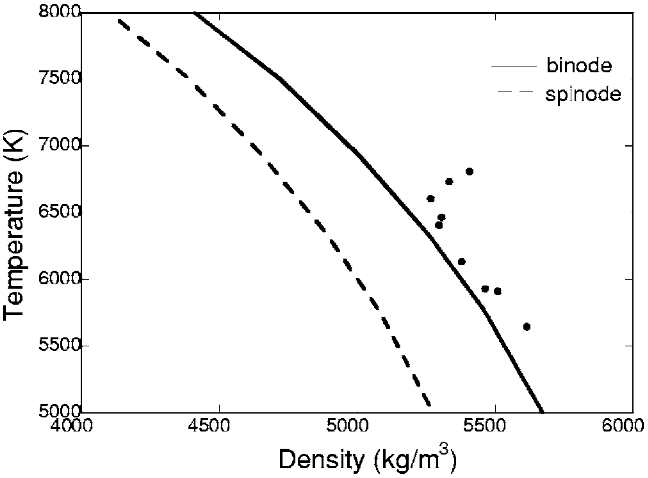

FIG. 16. Positions of groups of atoms on T-ρ diagram at 45 ps at laser fluence of 0.25 J/cm^2.

One factor that facilitates phase explosion is the tensile stress generated by laser heating. When the material is heated by a laser pulse, its density decreases, which is mainly due to the thermal expansion resulting from laser heating. However, the propagation of the stress wave induced by laser heating also has an effect on the density profile. As shown in Fig. 7(b), there is a tensile stress after the strong compressive wave passes. In Fig. 17, this tensile stress and the atomic number density for the fluence of 0.3 J/cm^2 are plotted together. The time step of 36 ps is chosen because gas bubbles are generated about 3 ps later. At the surface, the tensile stress remains at zero (as it should be according to the requirement of force balance). Under the surface, the increase of the tensile stress tends to decrease the density. On the other hand, the decrease of temperature tends to increase the density. The combined effect is that the minimum density is reached below the surface, where the material located is more likely to reach the spinode line and undergo the phase change process. This explains why the gas bubble appears not at the surface, but under the surface as shown in Fig. 5.

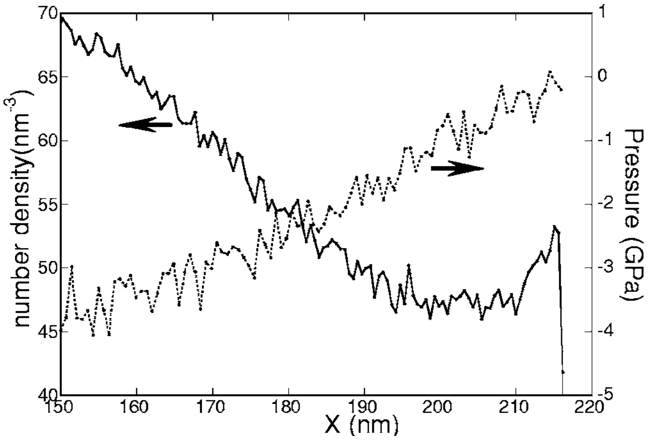

FIG. 17. Profile of pressure and atomic number density at 36 ps at laser fluence of 0.3 J/cm^2.

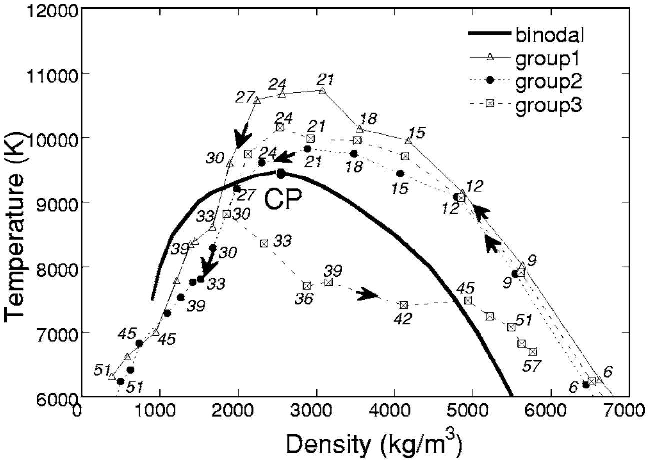

FIG. 18. Thermodynamic trajectories of atoms groups. Fluence, 0.65 J/cm^2.

B. Ablation at high laser fluences

Similar to the preceding section, the mechanism leading to ablation at higher laser fluences is also analyzed from the thermodynamic trajectories of groups of atoms.

Figure 18 shows the thermodynamic trajectories of several groups of atoms. The locations of these groups of atoms at 90 ps are marked in Fig. 19. The laser fluence is 0.65 J/cm^2. From Fig. 18, it is seen that all the three groups are first raised to temperatures higher than the critical temperature and become a super-critical fluid. After expansion, their temperature decreases, and they enter the unstable zone below the critical point as the phase separation occurs at about 30 ps. Groups 1 and 2 evolve into gas, while group 3 becomes liquid. Comparison between Figs. 5 and 18 shows that there is no phase separation during the initial heating period (from 1 ps to about 30 ps) although the density decreases continuously. The material remains homogeneous until it enters the unstable zone after expansion, and the liquid (group 3) precipitates out from the homogeneous phase. Similarly to Fig. 15, the velocity distributions of groups 2 and 3 at different time steps leading to ablation are plotted and compared with the equilibrium Maxwell-Boltzmann distribution to verify the local thermal equilibrium condition. Again, velocities of atoms are found to follow the equilibrium distribution, indicating that local thermal equilibrium is achieved. (See Fig. 20.)

The thermodynamic trajectories of the groups of atoms described above are clearly different from those at lower laser fluences, but follow that of critical point phase separation shown in Fig. 2(a). Heating above the critical point, followed by the expansion into the unstable zone that causes phase separation has been clearly illustrated, which agrees

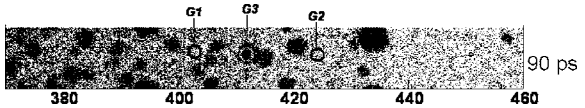

FIG. 19. Positions of groups of atoms on T-ρ diagram at 90 ps at laser fluence of 0.65 J/cm^2.

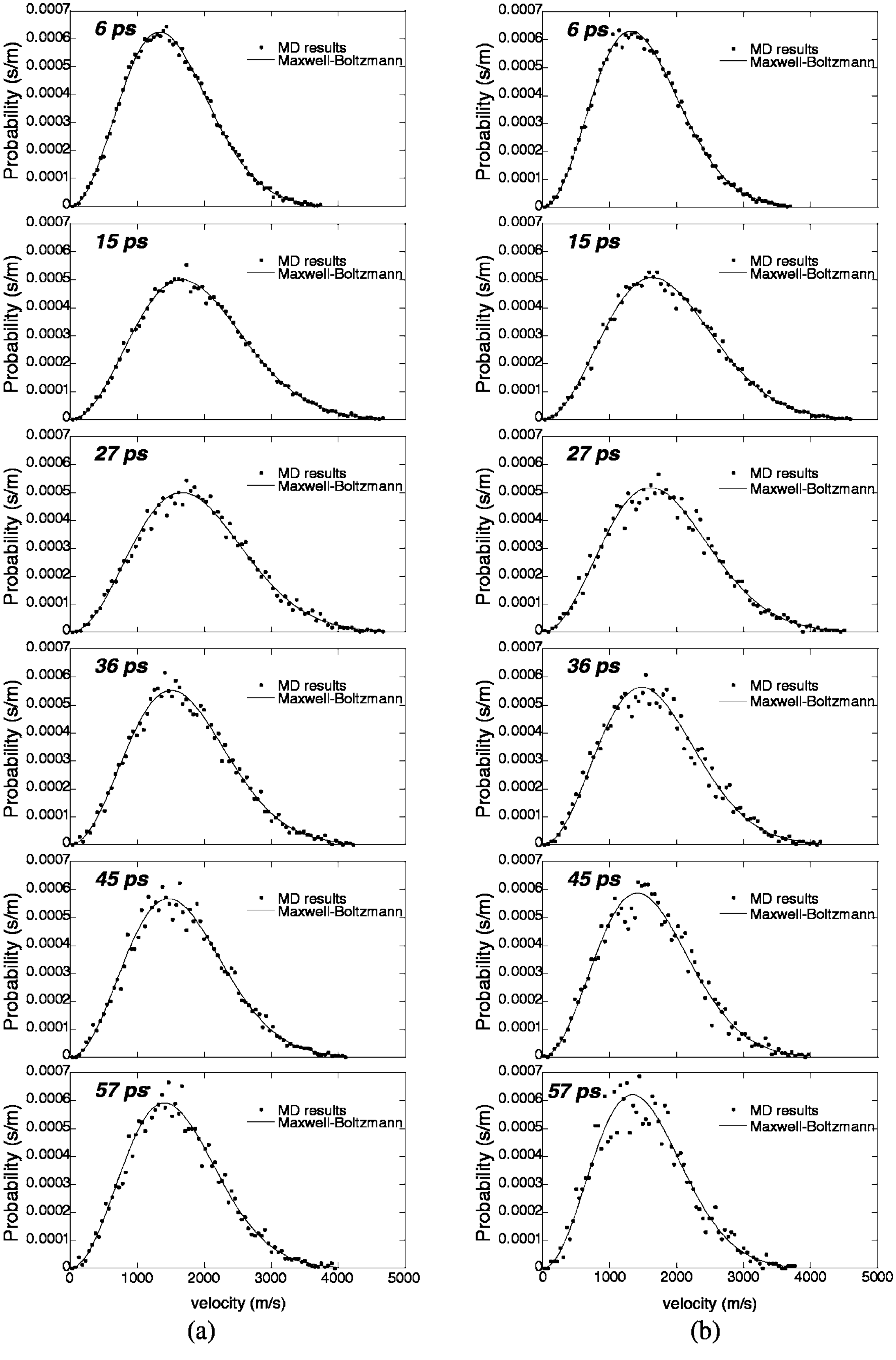

FIG. 20. Velocity distributions for (a) group 3 and (b) group 2 in Figs. 18 and 19.

with the theoretical description of critical point phase separation. Similar thermodynamic trajectories are found for laser fluences of 1.0 $\mathrm{J/cm^2}$ and 1.5 $\mathrm{J/cm^2}$. Therefore, it is concluded that critical point phase plays important roles in material decomposition.

V. SUMMARY

In this work, the mechanisms of femtosecond laser ablation of a nickel target are studied using molecular dynamic simulations in a laser fluence range commonly used for materials processing. Two distinct laser fluence regimes are identified, which are caused by different ablation mechanisms. At lower laser fluences, the peak temperature reached is below the critical temperature, and material decomposition is through phase explosion. Bubble nucleation occurs inside the metastable liquid at temperatures as the spinode is approached, and is assisted by the tensile stress developed during laser heating. At higher laser fluences critical point phase separation occurs. The initial peak temperature reached exceeds the critical temperature. The super-critical fluid enters the unstable zone after relaxation and loses its homogeneity, causing phase separation.

ACKNOWLEDGMENTS

Support of this work by the National Science Foundation Grant No. 0219098-CTS is acknowledged. C.C. also thanks the Fellowship support from the Purdue Computational Research Institute.

---

*Author to whom correspondence should be addressed. Electronic address: xxu@ecn.purdue.edu

[1] D. von der Linde and K. Sokolowski-Tinten, Appl. Surf. Sci. **154–155**, 1 (2000), and references therein.
[2] F. Korte, J. Serbin, J. Koch, A. Egbert, C. Fallnich, A. Ostendorf, and B. N. Chichkov, Appl. Phys. A: Mater. Sci. Process. **A77**, 229 (2003).
[3] R. Kelly and A. Miotello, Appl. Surf. Sci. **96–98**, 205 (1996).
[4] K. H. Song and X. Xu, Appl. Surf. Sci. **127**, 111 (1998).
[5] J. H. Yoo, S. H. Jeong, X. L. Mao, R. Grief, and R. E. Russo, Appl. Phys. Lett. **76**, 783 (2000).
[6] L. V. Zhigilei, Appl. Phys. A: Mater. Sci. Process. **A76**, 339 (2003).
[7] D. Perez and L. J. Lewis, Phys. Rev. Lett. **89**, 255504 (2002).
[8] P. Lorazo, L. J. Lewis, and M. Meunier, Phys. Rev. Lett. **91**, 225502 (2003).
[9] K. Sokolowski-Tinten, J. Bialkowski, A. Cavalleri, D. von der Linde, A. Oparin, J. Meyer-ter-Vehn, and S. I. Anisimov, Phys. Rev. Lett. **81**, 224 (1998).
[10] D. Perez and L. J. Lewis, Phys. Rev. B **67**, 184102 (2003).
[11] X. Xu, in *Annual Review of Heat Transfer*, edited by C.-L. Tien, V. Prasad, and F. P. Incropera (Bell House, New York, 2001), Vol. 12, p. 79.
[12] V. P. Skripov and A. V. Skripov, Sov. Phys. Usp. **22**, 389 (1979).
[13] L. A. Girifalco and V. G. Weizer, Phys. Rev. **114**, 687 (1959).
[14] S. M. Foiles, M. I. Baskes, and M. S. Daw, Phys. Rev. B **33**, 7983 (1986).
[15] W. K. Liu, J. M. Yuan, and S. H. Lin, Phys. Rev. A **60**, 1363 (1999).
[16] E. Ohmura, I. Fukumoto, and I. Miyamoto, Proc. SPIE **4088**, 84 (2000), and references therein.
[17] V. Constantoudis and C. A. Nicolaides, Phys. Rev. E **64**, 056211 (2001).
[18] N. N. Nedialkov, S. E. Imamova, and P. A. Atanasov, J. Phys. D **37**, 638 (2004).
[19] M. P. Allen and D. J. Tildesley, *Computer Simulation of Liquids* (Clarendon, Oxford, 1987).
[20] X. Wang and X. Xu, Int. J. Heat Mass Transfer **46**, 45 (2002).
[21] C. Cheng and X. Xu, Appl. Phys. A: Mater. Sci. Process. **A79**, 761 (2004).
[22] J. M. Haile, *Molecular Dynamics Simulation: Elementary Methods* (Wiley, New York, 1992).
[23] X. Wang and X. Xu, ASME J. Heat Transfer **124**, 265 (2002).
[24] C. Schäfer, H. M. Urbassek, L. V. Zhigilei, and B. J. Garrison, Comput. Mater. Sci. **24**, 421 (2002).
[25] J. Hohlfeld, S.-S. Wellershoff, J. Güdde, U. Conrad, V. Jähnke, and E. Matthias, Chem. Phys. **251**, 237 (2000).
[26] S. I. Anisimov, B. L. Kapeliovich, and T. L. Perel'man, Sov. Phys. JETP **39**, 375 (1974).
[27] T. Q. Qiu and C. L. Tien, J. Heat Transfer **115**, 835 (1993).
[28] T. Q. Qiu and C. L. Tien, Int. J. Heat Mass Transfer **37**, 2789 (1994).
[29] S. S. Wellershoff, J. Hohlfeld, J. Güdde, and E. Matthias, Appl. Phys. A: Mater. Sci. Process. **A69**, S99 (1999).
[30] P. A. Atanasov, N. N. Nedialkov, S. E. Imamova, A. Ruf, H. Hügel, F. Dausinger, and P. Berger, Appl. Surf. Sci. **186**, 369 (2002).
[31] D. R. Lide, *Handbook of Chemistry and Physics*, 77th ed. (CRC Press, Boca Raton, FL, 1996).
[32] H. Häkkinen and U. Landman, Phys. Rev. Lett. **71**, 1023 (1993).
[33] D. S. Ivanov and L. V. Zhigilei, Phys. Rev. B **68**, 064114 (2003).
[34] R. Berman, *Thermal Conduction in Solids* (Clarendon, Oxford, 1976).
[35] D. A. Young and B. J. Alder, Phys. Rev. A **3**, 364 (1971).
[36] M. M. Martynyuk, Russ. J. Phys. Chem. **57**, 810 (1983).
[37] D. A. Young, UCRL-52352, Lawrence Livermore Laboratory, 1977.